Hydrol. Earth Syst. Sci. Discuss., 8, 2895–2928, 2011
www.hydrol-earth-syst-sci-discuss.net/8/2895/2011/
doi:10.5194/hessd-8-2895-2011

Hydrology and Earth System Sciences Discussions

This discussion paper is/has been under review for the journal Hydrology and Earth System Sciences (HESS). Please refer to the corresponding final paper in HESS if available.

Estimating flooded area and mean water level using active and passive microwaves: the example of Paraná River Delta floodplain

M. Salvia[1], F. Grings[1], P. Ferrazzoli[2], V. Barraza[1], V. Douna[1], P. Perna[1], and H. Karszenbaum[1]

[1]Instituto de Astronomía y Física del Espacio (IAFE), Ciudad Universitaria, Pabellón IAFE, Buenos Aires, Argentina
[2]Tor Vergata University, Ingegneria, DISP, 00133 Rome, Italy

Received: 27 December 2010 – Accepted: 3 January 2011 – Published: 21 March 2011

Correspondence to: F. Grings (verderis@iafe.uba.ar)

Published by Copernicus Publications on behalf of the European Geosciences Union.

Abstract

This paper describes a procedure to estimate both the fraction of flooded area and the mean water level in vegetated river floodplains by using a synergy of active and passive microwave signatures. In particular, C Band Envisat ASAR in Wide Scan mode and AMSR-E at X, Ku and Ka Band, are used. The method, which is an extension of previously developed algorithms based on passive data, exploits also model simulations of vegetation emissivity. The procedure is applied to a long flood event which occurred in the Paraná River Delta from December 2009 to April 2010. Obtained results are consistent with in situ measurements of river water level.

1 Introduction

Over the past decade, several flood monitoring/forecast methodologies, based on remote sensing data, have been proposed. Among them, the ones based on microwave observations are the most successful, since large flood events and intense cloud covers are often encountered simultaneously. Furthermore, since flood events are strong dynamic processes, higher temporal resolutions are required, even if this leads to lower spatial resolutions. Therefore, passive microwaves are often exploited. This is particularly true in the large river basins, where extreme flood events compromise thousands of square kilometers in a few days.

From a physical point of view, the sensitivity of microwave measurements to soil and vegetation properties was proved by several theoretical and experimental investigations (Ulaby et al., 1986). In many cases, passive microwave investigations adopt the absolute difference between the vertically and horizontally polarized brightness temperatures ΔT (Choudhury, 1989). In other cases, the same difference is normalized to the average value PI (Paloscia et al., 1993) with the advantage to reduce, or eliminate at all, the dependence on surface temperature. For angles higher than 30°–40°, it was proved that both ΔT and PI are high for wet, flat and bare soils, while their values are reduced if the soil is dry, and in presence of roughness and/or vegetation cover (Ulaby et al., 1986; Choudhury, 1989; Kerr and Njoku, 1990; Paloscia et al., 1993; Jackson and Schmugge, 1991; Paloscia and Pampaloni, 1988; Ferrazzoli et al., 1992). All the effects produced by flooding contribute to an increase of ΔT and PI. For moderate water levels, flooding increases the moisture of the surface and decreases its roughness. For high water levels, and in presence of vegetation cover, flooding also reduces the height of the emerged vegetation. Therefore, the polarization indexes have the potential to detect the fraction of inundated area and to monitor the increase of water level. Finally, it is important to mention that these effects are present at all microwave frequencies. Lower frequencies show a better dynamics, but are characterized by lower spatial resolution.

The influence of soil and vegetation variables on radar signatures was also investigated extensively. For the active microwave case, the overall backscattering coefficient is essentially influenced by three processes: surface direct contribution, vegetation contribution and surface-vegetation double bounce. At lower frequencies (L, C and X Band) and angles higher than about 30°, the three contributions behave and interact in a complex way. Surface backscattering increases with moisture and roughness. Vegetation attenuates surface backscattering and produces its own contribution, as well as double bounce. Flooding reduces the surface contribution, due to the decrease of roughness, and increases the double bounce effect in vegetated areas. At C Band, the overall effect produced by a moderate flooding is an increase of the backscattering coefficient due to an increase of the double bounce contribution. However, if the increase of water level submerges most of the vegetation cover, the overall effect is a decrease of backscattering coefficient. Therefore, the trend of the backscattering coefficient as a function of water level is not monotonic. These properties have been investigated for some cases of agricultural and natural vegetation, mostly at C and X Band, also with the aid of models (Le Toan et al., 1989; Caizzone et al., 2009; Grings et al., 2005). The increase of the backscattering coefficient during flooding, related to double bounce, was detected also in forest cover areas, using L Band signatures (Wang et al., 1995).

The above mentioned properties make microwave remote sensing an ideal candidate for flood monitoring of large river basins. Some algorithms were designed to integrate both active and passive information in order to estimate flood conditions. A global study about flood dynamics was carried out using SSM/I signatures in synergy with data collected by AVHRR and ERS scatterometer (Prigent et al., 2007).

However, most of the operational algorithms still use only passive or active data. Several authors proposed methodologies to estimate flooded area as a function of brightness temperature (or derived indexes) and ancillary information. In Choudhury (1989) the sensitivity of the polarization difference (ΔT) measured at Ka Band to flood events was investigated. Nimbus 7 data was used to monitor the Amazon River, and a strong seasonal pattern partially correlated to river water level was found.

An operational algorithm based on passive microwave data which estimates the fraction of flooded area was developed by Sippel et al. (1994) and further used in Sippel et al. (1998) and Hamilton et al. (2002). Using physical hypotheses about the emissivity of water and vegetation, this algorithm estimates the fraction of flooded area of a pixel as a function of the absolute polarization difference (ΔT) at a given frequency. The fractional flooded area is estimated using linear mixing models that account for the microwave emission of the major land covers within the subregion (Sippel et al., 1994). This algorithm was tested using Ka Band of SSM/I system. It assumes that the temperature difference of flooded land, ΔT_f, has a constant value for all the flooded vegetation types present in the area. This assumption is critical, since ΔT_f can present large variations as reported by Sippel et al. (1994, 1998), Hamilton et al. (2002). In part, these variations are simply related to the statistical inhomogeneity of vegetation cover in the dimension of the spaceborne radiometer pixel, which is of the order of hundreds of km^2. However, they are also physically related to variations of water level in vegetated areas, as previously observed in Sippel et al. (1998), Hamilton et al. (2002). Moreover, this dependency on water level is related to vegetation structure; in fact, for wetland marshes, an increase in water level corresponds to a proportional decrease in the emerged biomass, with severe effects on the vegetation emissivity. On

HESSD
8, 2895–2928, 2011

the contrary, in arboreous vegetation an increase in water level is related to a decrease in trunk height, a component of the vegetation that has negligible emission properties for frequencies ≧6.9 GHz.

The objective of this paper is to estimate both the fraction of inundated area and the mean water level inside a wetland. The Paraná River Delta is selected as test site. The work adopts techniques of previous papers, such as the formulas of Sippel et al. (1994) and an interaction model that simulates the vegetation polarization difference as a function of water level. The general approach is based on the use of both active and passive signatures, collected almost simultaneously. First of all, the fraction of inundated area is evaluated by applying a threshold technique to Envisat-ASAR signatures collected in the Wide Swath (WS) mode. Then, AMSR-E signatures are used and formulas of Sippel et al. (1994) are inverted, in order to evaluate the ΔT_f value. Finally, the average water level is estimated by inverting the results of model simulations. In this procedure three AMSR-E channels, i.e. X, Ku and Ka Band, are tested. C Band is not considered, due to its poor spatial resolution. Some empirical corrections are used to remove the effects of the continental area.

Section 2 gives details about the study area and the used satellite signatures. Moreover, it describes all the details of the adopted procedure. The obtained results are shown and commented in Sect. 3.

2 Materials and methods

2.1 Description of the site and available maps

The Paraná River Delta (PRD) region stretches through the final 300 km of the Paraná basin. It covers approximately 17 500 km^2, close to Buenos Aires city in Argentina. A land cover map is shown in Fig. 1.

The Paraná River drains an approximate area of 2 310 000 km^2 and, according to its length, basin size, and water discharge, is considered the second most important

HESSD
8, 2895–2928, 2011

one in South America after the Amazonas. Among the large rivers of the world, it is the only one that flows from tropical to temperate latitudes, where it joins the Uruguay River ending in the Del Plata estuary.

The landscape patterns of this region are subordinated to a flooding regime characterized by different sources of water with different properties, such as local precipitation and large rivers, whose specific flooding patterns affect particular areas. Sometimes these sources add together provoking strong flooding events. The greatest influence comes from the Paraná River, which shows a main flood peak in late summer and a second peak in winter.

The combination of local topographic gradients and a regional flooding regime constitutes the primary factor that determines the emergent natural vegetation, mainly consisting of marshes growing in lowlands where the substrate is saturated permanently or semi permanently (Parmuchi et al., 2002). In the specific area of the Delta under study, there are four ecosystems that account for more than 95% of the landcover: junco marsh, cortadera marsh, grassland and prairie of aquatic herbaceous vegetation. All these ecosystems are composed by herbaceous vegetation, which presents an average height of 2 m. Some of them (cortadera marsh, grassland) are mainly composed by leafy vegetation with nearly uniform density and an average LAI of ~5. The other ones (junco marsh, praire) are composed by nearly vertical long stems, with an average density of ~90 plants/m^2. The selected area is indicated as a rectangle in Fig. 1. It includes a significant fraction of the Delta. For operational reasons, which will be explained later, also a continental part is considered, but its contribution will be subtracted. Therefore, the part of the Delta where the fraction of flooded area and the mean water level as a function of time will be evaluated is dominated by two marsh species: Junco (*Schoenoplectus californicus*), and Cortadera (*Scirpus giganteus*) (Salvia et al., 2009).

HESSD
8, 2895–2928, 2011

2.2 Available data

To estimate the hydrological condition of this area, we used both active and passive microwave signatures, as well as ancillary data. In particular, we used Wide Swath Envisat ASAR data and brightness temperature AMSR-E data. Details about product characteristics are given in Table 1.

Seven acquisition dates were available for ASAR data. They are, in Julian days starting from 1 January 2009: 161, 231, 264, 336, 353, 371 and 476. The first date, which corresponds to non flooded conditions, was selected as a reference. A change detection algorithm was applied to the subsequent six acquisitions. The corresponding six AMSR-E dates were selected in order to be as close as possible to ASAR ones, with the further condition to be separated by multiples of 16 days, which corresponds to the repeat orbit. Following these criteria, the selected AMSR-E Julian dates are: 232, 264, 328, 344, 376 and 472.

AMSR-E is a microwave radiometer operating at six frequency bands: 6.925 GHz (C), 10.65 GHz (X), 18.7 GHz (Ku), 23.8 GHz, 36.5 GHz (Ka), and 89.0 GHz (Kawanishi et al., 2003; Parkinson, 2003). A conical scanning is used to observe the terrestrial surface with a local angle of 55°. The IFOV is dependent on frequency. In order to compare among different bands, in this work we used products with the resolution of X Band, i.e. AMSR-E Res-2, 29 × 51 km, for all channels. For the higher frequencies (Ku and Ka Band) we used data resampled to this resolution. The data are stored in Hierarchical Data Format (HDF), which is compatible with NASA HDF-EOS standard. In this study, we used L1b data, which contains values of brightness temperature, at vertical (V) and horizontal (H) polarization, corrected and calibrated. Each file is 80 Mb, contains brightness temperature values along a 1450 km strip. The data was downloaded from NASA site (https://wist.echo.nasa.gov/~wist/api/).

Even when using 16-days repeat orbit data, the centers of AMSR-E image pixels are not coincident. This is due to AMSR-E conical scanning acquisition strategy (Kawanishi et al., 2003). Therefore, it is not possible to perform a pixel to pixel comparison between

HESSD
8, 2895–2928, 2011

two images, even if they are from the same orbit. Instead, a drop-in-the-bucket method is usually preferred in time series analysis of AMSR-E data (Kawanishi et al., 2003). This method estimates the mean value of the brightness temperature of an area as the average of all the observations whose pixel centers are contained in this area. However, it is important to remark that this estimate includes brightness temperature observations from outside the area of interest. This error can be neglected when the study area is large and homogeneous, but is critical when comparing multitemporal data corresponding to a small area (i.e. a narrow river floodplain). Furthermore, these errors are proportional to sum of the fractions of footprint areas that are outside the study area. In our case, since the area is narrow and the polarization difference of the wetland is large compared to the one of the continent, the overall effect is a reduction of the observed polarization difference.

In order to deal with this issue, we developed an ad hoc strategy to minimize the effects of this kind of errors in small areas. To this end, we extracted AMSR-E data from the rectangular box indicated in Fig. 1, which is larger than the specific study area limited by the Delta, since it includes a known fraction of the continent. Then, we developed a methodology to estimate the polarization differences specifically contributed by the Delta area. To this aim, we used the polarization difference values averaged over the whole box of Fig. 1 and over some sample areas taken within the continent.

Multitemporal images of the observed polarization difference ΔT_{obs} at X Band are shown in Fig. 2. An evident increase of the polarization difference is observed after December 2009.

As far as active microwave signatures are concerned, this work uses ENVISAT ASAR precision image products in Wide Swath image mode (ESA, 2007). For each date, there is a multilook ground range digital image. For this particular application, we selected HH polarization, considering the well known dynamic range of HH to changes in flood condition (Grings et al., 2005). Sample images of the area are shown in Fig. 3. The first image was collected on 6 October 2009, corresponding to a non-flooded condition, and was used as a reference. An evident change of the backscattering coefficient is observed in the subsequent two images. It is an increase for moderate flooding, and a decrease for intense flooding, as discussed in Grings et al. (2006).

In order to interpret the changes in the backscattering coefficient and in brightness temperature, we used both the landcover map of Fig. 1 and ancillary data. Among them, water level information is important. Figure 4 shows the trend of this variable measured at Rosario port station, located in the Delta. A significant change in the hydrological condition of the watershed is observed. In the figure, the acquisition dates of the AMSR-E images are marked with vertical lines. The water level corresponding to the alert level for the Delta in Rosario is marked with a horizontal line. The alert level (the level for which the River starts to inundate the floodplain) was reached for a Julian date between 336 (2 December 2009) and 353 (19 December 2009). This produced effects on both passive and active signatures, as can be detected in Figs. 2 and 3.

2.3 Basic formulas

Basically, the passive data have been analyzed using the simple model proposed by Sippel et al. (1994). The model has three end-members, that represent the contributions of water, non-flooded land, and inundated floodplain to the total observed polarization difference ΔT_{obs},

$$\Delta T_{\mathrm{obs}} = f_{\mathrm{w}}\Delta T_{\mathrm{w}} + f_{\mathrm{nf}}\Delta T_{\mathrm{nf}} + f_{\mathrm{f}}\Delta T_{\mathrm{f}} \tag{1}$$

$$1 = f_{\mathrm{w}} + f_{\mathrm{f}} + f_{\mathrm{nf}} \tag{2}$$

where ΔT_{obs} is the polarization difference observed by the radiometer, f_{w}, f_{nf} and f_{f} are the fractional areas of open water (rivers and lakes without emergent vegetation), non-flooded land, and seasonally flooded land, respectively, and ΔT_{w}, ΔT_{nf}, and ΔT_{f} are the polarization difference values for open water, non-flooded land, and seasonally flooded land, respectively. Simultaneous solution of Eqs. (1) and (2) yields the following

HESSD
8, 2895–2928, 2011

Estimating flood condition from microwave data

M. Salvia et al.

equation for the fraction of inundated floodplain (f_f):

$$f_\mathrm{f} = \frac{\Delta T_\mathrm{obs} - f_\mathrm{w}\Delta T_\mathrm{w} - \Delta T_\mathrm{nf} + f_\mathrm{w}\Delta T_\mathrm{nf}}{\Delta T_\mathrm{f} - \Delta T_\mathrm{nf}} \tag{3}$$

The fractional area of flooded land expands during inundation with a concomitant reduction in the fractional area of non-flooded land. The algorithm is based on the following hypothesis:

1. The temperature difference of water bodies at a given frequency, ΔT_w, is constant and known.
2. The temperature difference of non-flooded land, ΔT_nf, is constant and shows a unique value for all the vegetation types present in the area and can be estimated from images.
3. The fractional area of permanent water bodies is constant and known.
4. The temperature difference of flooded land, ΔT_f, is constant, shows a unique value for all the vegetation types present in the area, and can be estimated from images.

2.4 Model simulations

As it will be outlined in Sect. 2.5.6, we use a look-up table which associates ΔT_f to water level (WL), for all the considered AMSR-E channels. The look-up table is obtained by model simulations. We used the vegetation model developed at Tor Vergata University. It is a discrete model based on the radiative transfer theory, including multiple scattering effects. The model is able to compute both the emissivity and the backscattering coefficient, and was adapted to several types of vegetation. Details of the passive version are available in Ferrazzoli and Guerriero (1996a,b). In the study area, the main vegetation is herbaceous, and the main species are junco and cortadera. For this type of vegetation, we adopted the vegetation dielectric and geometric characteristics

HESSD
8, 2895–2928, 2011

already used in Grings et al. (2006) to simulate the changes in the backscattering coefficient of the herbaceous vegetation due to changes in the flood condition. The soil is represented as a half-space with rough interface. For inundated marshes, the soil has the permittivity of water and a low roughness. For junco marshes, vegetation elements are stems, represented as vertical dielectric cylinders. Their height is equal to the height of the emerged vegetation, while other variables are given on the basis of previous measurements (Grings et al., 2006, 2008). For cortadera marshes, which are essentially made of long leaves, vegetation elements are represented as dielectric discs. The maximum leaf area index in absence of flooding is equal to 5. While the water level increases, the leaf area index is assumed to be reduced following a linear trend, consistent with the uniform distribution of biomass observed experimentally. The other variables are also assigned on the basis of previous measurements (Grings et al., 2006). The input variables to the model are given in Table 2.

2.5 Methodology

In order to deal with drop-in-the-bucket inherent errors associated to small areas already mentioned in Sect. 2.2, we developed a methodology to extract the polarization difference values of Paraná River delta area from a known larger area. This methodology is necessary, since it is not possible to have the same pixel centers at all dates, even using repeat pass orbit images. Moreover, the included area of continent varies from image to image and introduces several artifacts that degrade the quality of the estimation of the flooded fraction. In fact, the averaging is affected by the contribution of border pixels mainly dominated by crops, which present a low polarization difference.

In order to solve this issue, we have selected an area larger than the river floodplain (see Fig. 1). For the rectangular box indicated in Fig. 1, we analyzed the data according to a method consisted of several steps.

1. The fraction of flooded area was estimated using ASAR;
2. The average polarization difference ΔT_{obs} was computed using AMSR-E signatures at X, Ku and Ka Band;
3. The contribution of the continental part of the rectangular box was removed;
4. For all frequencies, the contributions of non-flooded areas ΔT_{nf} and water bodies ΔT_{w} were estimated;
5. The polarization difference ΔT_{f} in flooded delta was estimated;
6. Inverting a look up table based on model simulations, ΔT_{f} values were converted into corresponding water level (WL) values.

The various steps of the procedure are described below.

2.5.1 Estimation of the fraction of flooded area f_f

The fraction of flooded area is estimated from pairs of Envisat ASAR WS images. The first image of the pair is the reference one collected on Julian day 161, that is in a dry period, and the second one was collected in six different dates during the flooding. The change of the backscattering coefficient (σ^0) between images was associated to a change in the hydrological condition. There are previous results that support this statement in wetland marshes worldwide (Hess et al., 1995) and in particular, in Paraná River wetland marshes observed by Envisat ASAR (Grings et al., 2005, 2009; Salvia et al., 2009).

Since the complete flood event we are analyzing lasted 9 months, we compared images from different seasons. Therefore, one important hypothesis is that C Band σ^0 of the studied vegetation does not depends strongly on season; therefore, the changes in C Band σ^0 can be univocally interpreted as changes in the flood condition. For the Paraná River Delta marshes, that are perennial, there is experimental evidence

HESSD
8, 2895–2928, 2011

that the C Band σ^0 of the vegetation measured with Envisat ASAR does not change significantly between seasons (Pratolongo, 2005).

According to previous works, in predominantly vertical wetland marshes observed at C Band, a change in the flood condition can produce either an increase or a decrease in the overall σ^0 of the area (Grings et al., 2008). This is due to a complex interaction between vegetation bistatic scattering and vegetation attenuation (Grings et al., 2006). In fact, flooding reduces the surface contribution, due to the decrease of roughness, but increases the double bounce. Overall, moderate flooding produces an increase of backscattering coefficient, due to the increase of double bounce. However, if the increase of water level submerges most of vegetation cover, the overall effect is a decrease of backscattering coefficient. Speckle should be considered in the change detection scheme. Since we are dealing with Wide Swath images (ENL~21, (ESA, 2007)), we selected as a compromise a threshold of 1.5 dB up and down. Therefore, all the areas that presented a positive or negative change with an absolute value higher than 1.5 dB with respect to the reference image were labeled as flooded (although possibly with different water levels).

2.5.2 Computation of the overall polarization difference ΔT_{obs}

For the three selected AMSR-E channels, and for all the listed dates the polarization difference ΔT_{obs}, was computed by averaging among all the pixels whose centers are inside the rectangular box of Fig. 1. These values resulted from a complex combination of various contributions: flooded marsh, non flooded marsh, water body and continental areas.

2.5.3 Removal of the continent part and estimation of the polarization difference of the wetland ΔT_{wet}

We estimated the polarization differences of the wetland, ΔT_{wet}, from the polarization differences of the original box, ΔT_{obs}. In order to remove the effect of the continent

HESSD
8, 2895–2928, 2011
Estimating flood condition from microwave data
M. Salvia et al.

contribution, we estimated the polarization difference of the continental part, ΔT_c, considering samples from both the Northeast and Southwest side of the river floodplain. Using this result, we estimated the polarization difference values of the wetland, ΔT_{wet}, as:

$$\Delta T_{wet} = \frac{\Delta T_{obs} - f_c \Delta T_c}{1 - f_c} \tag{4}$$

where f_c is the fraction of continent in the rectangular study area of Fig. 1. In order to estimate f_c, we subtracted the Paraná River Delta area to the total area (see Fig. 1). Using this procedure, we found f_c=0.51.

2.5.4 Estimation of non-flooded area (ΔT_{nf}) and water (ΔT_w) polarization differences

As stated before, the temperature difference of non-flooded land, ΔT_{nf} was considered constant for each frequency. In order to estimate this parameter from images, it is necessary to locate an homogeneously covered vegetated area of the dimension of the AMSR-E pixel in a non-flooded condition. Systematically analyzing high resolution images, no homogeneously covered vegetated pixel was found, due to the high heterogeneity present in the area. Therefore, we have taken ΔT_{nf} values as the values obtained from model simulations in the non-flooded case. Finally, we verified that these simulated values present good agreement with the AMSR-E measured values extracted in the drought period for nearly homogeneous vegetated pixels.

It is well established that the polarization difference of calm water, ΔT_w, depends on frequency, observation angle and surface roughness (Ulaby et al., 1986). We estimated this value for each frequency using the same AMSR-E images. To this end, we considered samples from a large permanent endorheic lake (Laguna de Mar Chiquita), located at a distance of about 300 km from the study site.

The obtained values of ΔT_w and ΔT_{nf} are summarized in Table 3.

HESSD
8, 2895–2928, 2011

2.5.5 Computation of the polarization difference in flooded marsh (ΔT_f)

As we discussed before, we assumed that the polarization differences of the flooded marshes, ΔT_f, cannot be considered constant for all dates and are in fact function of water level. Therefore, the formulas of Sippel et al. (1994) were used inversely, in order to estimate ΔT_f as a function of ΔT_{wet}. To this end, Eq. (1) was rewritten as:

$$\Delta T_f = \frac{\Delta T_{wet} - f_w \Delta T_w - \Delta T_{nf} + f_w \Delta T_{nf}}{f_f} + \Delta T_{nf} \tag{5}$$

In summary, we estimated ΔT_f, using the polarization differences of the wetland measured by AMSR-E (ΔT_{wet}), the flooded fraction of the wetland derived from Envisat ASAR data (f_f), the fraction of permanent water bodies derived from SAC-C data (f_w) (Salvia et al., 2009) and the polarization difference of water (ΔT_w) and non-flooded vegetation (ΔT_{nf}) given in Table 2.

2.5.6 Estimation of water level in flooded marsh (WL)

Finally, we estimated the water level as a function of the polarization difference of flooded marshes (ΔT_f), using a two-step procedure. The first step consisted in generating a look-up table which associated ΔT_f to water level (WL), for the considered AMSR-E channels. The second step essentially consisted in an inversion of the relationship defined previously. To establish the functional form of the dependence of ΔT_f on WL, we used the interaction model summarized in Sect. 2.4. For cortadera and junco marshes, the inputs of Table 2 were used. For cortadera marshes, an increase of water level produces a decrease of emerged Leaf Area Index with respect to its maximum value. For junco marshes, the emerged stem height decreases with water level. The total polarization difference was finally computed by averaging the contributions of junco and cortadera marshes. The results are presented in Fig. 5. As expected, ΔT_f increases with increasing water level. The slope is dependent on frequency and on the water level itself.

Then, in order to estimate the mean water level inside our study area, the relations of Fig. 5 were inverted. To this end, 2nd degree polynomials were fitted to the outputs of Fig. 5, so that an inverse relation between water level and ΔT_{f} was obtained for each frequency.

3 Results

Applying the procedure described in Sect. 2.5.1, we derived maps of flooded areas from ASAR images. For each SAR pixel, we considered the variations of backscattering coefficient with respect to the image of 10 June 2009, taken as a reference. For the six dates listed in Sect. 2.2, results are shown in Fig. 6.

As expected, the images corresponding to dates with higher river water level present a higher number of pixels with an increase or a decrease in the σ_0. As discussed in Sect. 2.5.1, we associate these variations to a change in the hydrological condition (from not flooded to flooded) inside the pixel. Considering all the pixels that present a change higher than 1.5 dB in absolute value as flooded pixels, we estimated the flooded fraction for the six images (Fig. 7). Due to the long term characteristics of this flooding process, the temporal variations are quite slow. The obtained values of f_{f} were associated to AMSR-E images collected in non coincident dates, although close, dates (see the corresponding list in Sect. 2.2). However, since the maximum temporal shift between ASAR and AMSR-E acquisitions was equal to 9 days and the temporal variations of f_{f} are slow, the errors associated to these shifts can be neglected.

Then, in order to estimate the ΔT_{wet} of the area of river basin under study, we applied the methodology described in Sects. 2.5.2 and 2.5.3. The obtained trends of ΔT_{obs}, ΔT_{c} and ΔT_{wet} as a function of time are shown in Fig. 8. The time is given in Julian dates, starting from 1 January 2009.

As expected, ΔT_{obs} (Fig. 8a) presents a complex behavior, related to the combined temporal trends of events both in the river floodplain and in the continent. The ΔT_{c} value, obtained from significant samples of the main continent landcover, shows its

HESSD
8, 2895–2928, 2011

own temporal trend mainly related to agricultural exploitation, particularly after Julian Day 330 (Late Spring in Argentina) (Fig. 8b). It can be seen that after the removal of the continent area, the ΔT_{wet} of the wetland area shows a generally increasing trend and an abrupt increase from Julian date 328 to Julian date 344 (Fig. 8c).

To estimate the ΔT_f values from ΔT_{wet} and f_f, we used Eq. (5) and the values of ΔT_{nf} and ΔT_w given in Table 3, according to the procedure described in Sect. 2.5.5. The results are shown in Fig. 9. It can be seen that the estimated ΔT_f trend shows a step between Julian Day 328 (24 November 2009) and Julian Day 344 (10 December 2009).

It can be seen that the estimated ΔT_f trend present near constant trends and a single step between Julian date = 328 (24 November 2009) and Julian date = 344 (10 December 2009).

Using the methodology depicted in Sect. 2.5.6 and the results of Fig. 5, we estimated the mean water level inside the study area as a function of ΔT_f. The results are shown in Fig. 10.

It is important to note that, even if the ΔT_f can present different trends for the same floodplain in the same hydrological condition (particularly X Band behaves differently from higher frequencies), the estimated trends of WL are similar for the three selected frequency channels (Fig. 10).

4 Conclusions

In this work, we presented a methodology to estimate the fraction of flooded area and the mean water level inside a wetland using active and passive microwave orbital systems. The methodology is based on the quasi-simultaneous measurements of the radiometric polarization difference and the differences of the backscattering coefficient with respect to a reference image. Using the differences of backscattering coefficients, the fraction of flooded area as a function of time was obtained. Then the polarization difference of the flooded vegetation was estimated and finally, with the aid of interaction models, the mean water level of the wetland area was obtained.

HESSD
8, 2895–2928, 2011

This methodology makes use of ancillary data, such as a landcover map that characterizes the main vegetation types present in the area, and exploits an interaction model that simulates the polarization difference of the vegetation at various frequencies and for different water levels.

A complete validation of the results over the whole area is not feasible. However, a comparison with in situ data of river water level measured at Rosario station is consistent. During the time in which the in situ measured water level increases, the fraction of flooded area increases regularly, while the water level estimated in the marshes increases slightly, with a step increment occurring in the Julian days from 328 to 344, when the river reached the alert level. Moreover, the algorithm was applied using three different AMSR-E frequencies showing very close values of mean water level. Although the behavior of ΔT_f at X Band differs from the other two, the trends of WL are similar.

The use of both active and passive data allows us to estimate also the water level in flooded vegetation, but limits the temporal resolution. As a future development, we plan to use the water level estimated using both passive and active signatures as an initial value in the algorithm of Sippel et al. (1994) that uses passive data only. This can allow us to exploit the temporal resolution of passive data with a periodic adjournment (using both passive and active data) of water level information.

Acknowledgements. The authors specially thank the European Space Agency (ESA) for the continuous support through AO 667 supported project, the National Commission for Space Activities (CONAE) for the optical data, the National Water Institute (INA) and the National Hydrologic Service (SHN) for providing us river water levels and precipitation data. This work was funded by the Agencia Nacional de Promocion Cientifica y Tecnologica (ANPCyT) (PICT 1203).

References

Caizzone, S., Ferrazzoli, P., Guerriero, L., and Pierdicca, N.: Modeling backscattering variations due to flooding over vegetated surfaces, Italian J. Remote Sens., 3, 2537 pp., 2009. 2897

Choudhury, B. J.: Monitoring global land surface using Nimbus-7 37 GHz data theory and examples, Int. J. Remote Sens., 10, 1579–1605, 1989. 2896, 2897, 2898

ESA: ASAR Product Handbook, Tech. rep., European Space Agency (ESA), 2007. 2902, 2907

Ferrazzoli, P. and Guerriero, L.: Passive microwave remote sensing of forests: a model investigation, IEEE T. Geosci. Remote, 34, 433–443, doi:10.1109/36.485121, 1996a. 2904

Ferrazzoli, P. and Guerriero, L.: Emissivity of vegetation: theory and computational aspects, J. Electromagnet. Waves, 1996b. 2904

Ferrazzoli, P., Guerriero, L., Paloscia, S., Pampaloni, P., and Solimini, D.: Modeling polarization properties of emission from soil covered with vegetation, IEEE T. Geosci. Remote, 30, 157–165, doi:10.1109/36.124226, 1992. 2897

Grings, F., Ferrazzoli, P., Karszenbaum, H., Tiffenberg, J., Kandus, P., Guerriero, L., and Jacobo-Berrles, J.: Modeling temporal evolution of junco marshes radar signatures, IEEE T. Geosci. Remote, 43, 2238–2245, doi:10.1109/TGRS.2005.855067, 2005. 2897, 2902, 2906

Grings, F., Ferrazzoli, P., Jacobo-Berlles, J., Karszenbaum, H., Tiffenberg, J., Pratolongo, P., and Kandus, P.: Monitoring flood condition in marshes using EM models and Envisat ASAR observations, IEEE T. Geosci. Remote, 44, 936–942, doi:10.1109/TGRS.2005.863482, 2006. 2903, 2905, 2907

Grings, F., Ferrazzoli, P., Karszenbaum, H., Salvia, M., Kandus, P., Jacobo-Berlles, J., and Perna, P.: Model investigation about the potential of C band SAR in herbaceous wetlands flood monitoring, Int. J. Remote Sens., 2008. 2905, 2907

Grings, F., Salvia, M., Karszenbaum, H., Ferrazzoli, P., Kandus, P., and Perna, P.: Advances in radar remote sensing of wetland ecosystems: Combination of satellite observations, field data and em Models, J. Environ. Manage., 90, 2189–2198, 2009. 2906

Hamilton, S., Sippel, S. J., and Melack, J. M.: Comparison of inundation patterns among major South American floodplains, J. Geophys. Res., 107, 2002. 2898

Hess, L., Melack, J., Filoso, S., and Wang, Y.: Delineation of inundated area and vegetation along the Amazon floodplain with the SIR-C synthetic aperture radar, IEEE T. Geosci. Remote, 33, 896–904, doi:10.1109/36.406675, 1995. 2906

Jackson, T. J. and Schmugge, T. J.: Vegetation effects on the microwave emission from soils, Remote Sens. Environ., 36, 203–212, 1991. 2897

Kawanishi, T., Sezai, T., Ito, Y., Imaoka, K., Takeshima, T., Ishido, Y., Shibata, A., Miura, M., Inahata, H., and Spencer, R.: The Advanced Microwave Scanning

Radiometer for the Earth Observing System (AMSR-E), NASDA's contribution to the EOS for global energy and water cycle studies, IEEE T. Geosci. Remote, 41, 184–194, doi:10.1109/TGRS.2002.808331, 2003. 2901, 2902

Kerr, Y. and Njoku, E.: A semiempirical model for interpreting microwave emission from semiarid land surfaces as seen from space, IEEE T. Geosci. Remote, 28, 384–393, doi:10.1109/36.54364, 1990. 2897

Le Toan, T., Laur, H., Mougin, E., and Lopes, A.: Multitemporal and dual-polarization observations of agricultural vegetation covers by X-band SAR images, IEEE T. Geosci. Remote, 27, 709–718, doi:10.1109/TGRS.1989.1398243, 1989. 2897

Paloscia, S. and Pampaloni, P.: Microwave polarization index for monitoring vegetation growth, IEEE T. Geosci. Remote, 26, 617–621, doi:10.1109/36.7687, 1988. 2897

Paloscia, S., Pampaloni, P., Chiarantini, L., Coppo, P., Gagliani, S., and Luzi, G.: Multifrequency passive microwave remote sensing of soil misture and roughness, Int. J. Remote Sens., 14, 467–483, 1993. 2896, 2897

Parkinson, C.: Aqua: an Earth-Observing Satellite mission to examine water and other climate variables, IEEE T. Geosci. Remote, 41, 173–183, doi:10.1109/TGRS.2002.808319, 2003. 2901

Parmuchi, G., Karszenbaum, H., and Kandus, P.: Mapping the Paraná River delta wetland using multitemporal RADARSAT/SAR data and a decision based classifier, Can. J. Remote Sens., 28, 175–186, 2002. 2900

Pratolongo, P.: Dinámica de comunidades herbáceas del bajo delta del río paraná sujetas a diferentes regímenes hidrológicos y su monitoreo mediante sensores remotos, Ph.D. thesis, Departamento de Ecología Genética y Evolución Facultad de Ciencias Exactas y Naturales Universidad de Buenos Aires, 2005. 2907

Prigent, C., Papa, F., Aires, F., Rossow, W. B., and Matthews, E.: Global inundation dynamics inferred from multiple satellite observations, 1993–2000, J. Geophys. Res., 112, 113–129, 2007. 2898

Salvia, M., Kandus, P., Karszenbaum, H., and Grings, F.: Optical and radar satellital data for mapping and monitoring wetland macrosystems, Rev. Esp. Teledeteccion, 31, 35–51, 2009. 2900, 2906, 2909, 2919

Sippel, S. J., Hamilton, S., Melack, J. M., and Choudhury, B.: Determination of inundation area in the Amazon River floodplain using the SMMR 37 GHz polarization difference, Remote Sens. Environ., 48, 70–76, 1994. 2898, 2899, 2903, 2909, 2912

HESSD

8, 2895–2928, 2011

Estimating flood condition from microwave data

M. Salvia et al.

Sippel, S. J., Hamilton, S., Melack, J. M., and Novo, E.: Passive microwave observations of inundation area and the area/stage relation in the Amazon River floodplain, Int. J. Remote Sens., 19, 3055–3074, 1998. 2898

Ulaby, F. T., Moore, R. K., and Fung, A.: Microwave Remote Sensing: Active and Passive, Vol. III – Volume Scattering and Emission Theory, Advanced Systems and Applications, Addison-Wesley, 1986. 2896, 2897, 2908

Wang, Y., Hess, L., Filoso, S., and Melack, J.: Understanding the radar backscattering from flooded and nonflooded Amazonian Forests: results from canopy backscatter modeling, Remote Sens. Environ., 54, 324–332, 1995. 2897

HESSD

8, 2895–2928, 2011

Table 1. Summary of used data.

	Envisat ASAR, Wide Swath Mode	AMSR-E
Pixel size	75 × 75 m	29 × 51 km
Operational Frequency	C Band	X, Ku and Ka Band
Available polarizations	HH	H and V
Acquisition dates	Non flooded: 10 Jun 2009 Flooded: 19 Aug 2009 21 Sep 2009 2 Dec 2009 19 Dec 2009 6 Jan 2010 21 Apr 2010	20 Aug 2009 21 Sep 2009 24 Nov 2009 10 Dec 2009 11 Jan 2010 17 Apr 2010

HESSD
8, 2895–2928, 2011

Estimating flood condition from microwave data

M. Salvia et al.

Table 2. Input parameters to the interaction model.

	Parameter	Value	Observations
General	Frequency	10.8 GHz, 18.7 GHz, 36.6 GHz	AMSR-E, X Band, Ku Band, Ka Band
	Incidence angle	55°	AMSR-E
Soil parameters	Soil moisture	$1.0\,cm^3/cm^3$	Flooded soil
	RMS height	0.04 cm	Flooded soil
	Correlation length	10 cm	Flooded soil
Vegetation parameters	Vegetation height	200 cm	Cortadera marsh
	Maximum emerged Leaf Area Index	5	Mean LAI of cortadera marsh
	Leaf width	2.5 cm	Cortadera marsh
	Leaf thickness	0.02 cm	Cortadera marsh
	Leaf gravimetric moisture	0.7 g/g	Cortadera marsh
	Maximum emerged stem height	180 cm	Junco marsh
	Stem radius	0.45 cm	Junco marsh
	Plant density	$90\,plants/m^2$	Junco marsh
	Stem gravimetric moisture	0.7 g/g	Junco marsh

HESSD
8, 2895–2928, 2011

Table 3. Parameters of the water level retrieval algorithm.

	ΔT_w (K)	ΔT_{nf} (K)
X Band	97	8.0
Ku Band	93	4.0
Ka Band	90	2.0

HESSD
8, 2895–2928, 2011

HESSD

8, 2895–2928, 2011

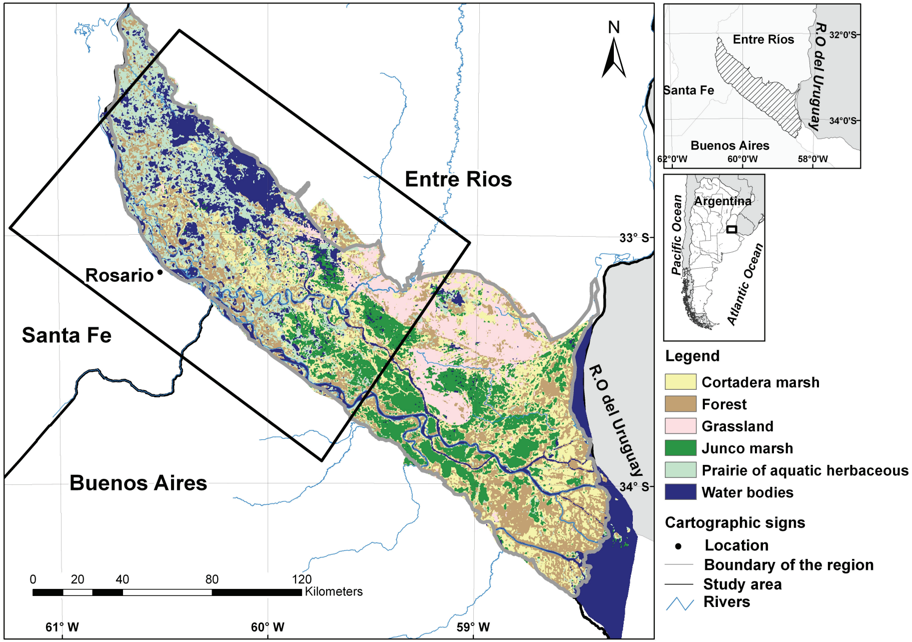

Fig. 1. Landcover map of Paraná River Delta. Main vegetation patterns mapped using SAC-C system (Salvia et al., 2009) are shown. The rectangular box indicates the area selected in this study.

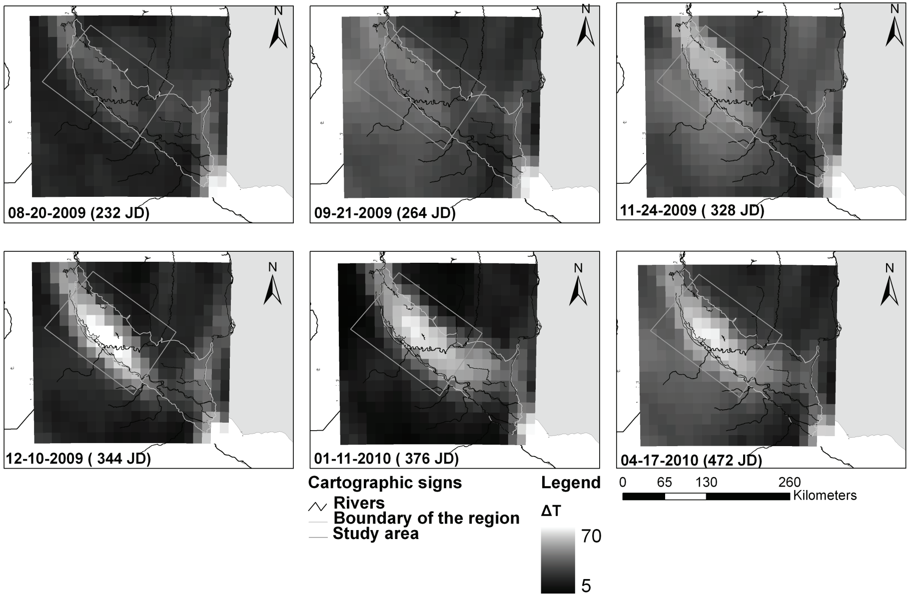

Fig. 2. AMSR-E images of ΔT at X Band in the Paraná River delta. Julian dates starting from 1 January 2009: 232, 264, 328 (upper figures), 344, 376, 472 (lower figures). The rectangular box indicates the area selected in this study.

HESSD
8, 2895–2928, 2011

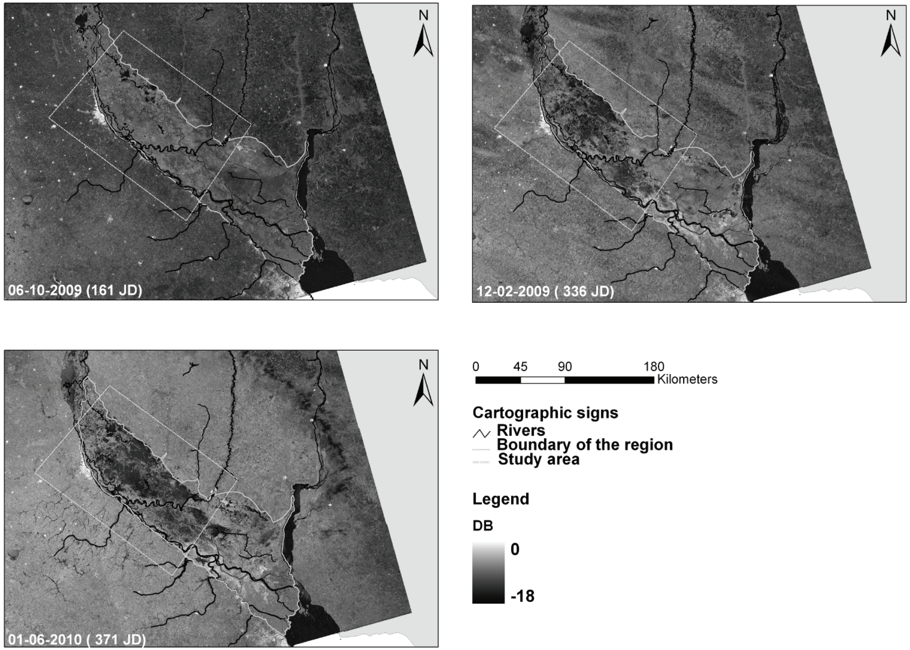

Fig. 3. Example of Envisat ASAR Wide Swath (HH polarization) images of the Paraná River delta used in this paper. Julian dates starting from 1 January 2009: 161, 336 (upper figures), 371 (lower figure). The rectangular box indicates the area selected in this study.

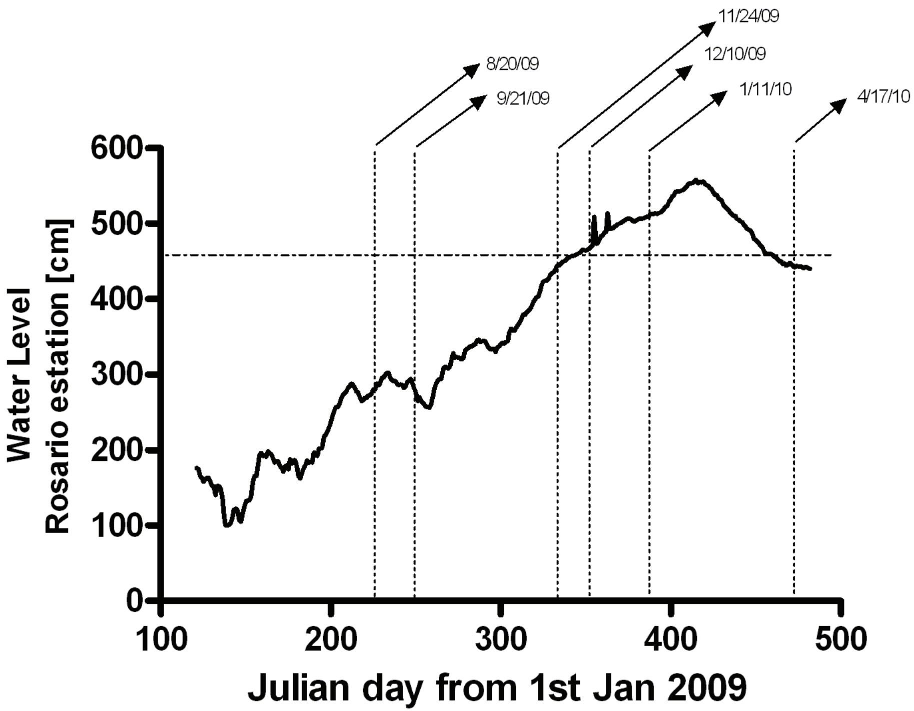

Fig. 4. Water level (cm) measured at Rosario city as a function of time. The horizontal line indicates alert river water level for Rosario city and vertical dotted lines indicate AMSR-E acquisition dates.

HESSD
8, 2895–2928, 2011

Estimating flood condition from microwave data

M. Salvia et al.

Title Page
Abstract Introduction
Conclusions References
Tables Figures
Back Close
Full Screen / Esc
Printer-friendly Version
Interactive Discussion

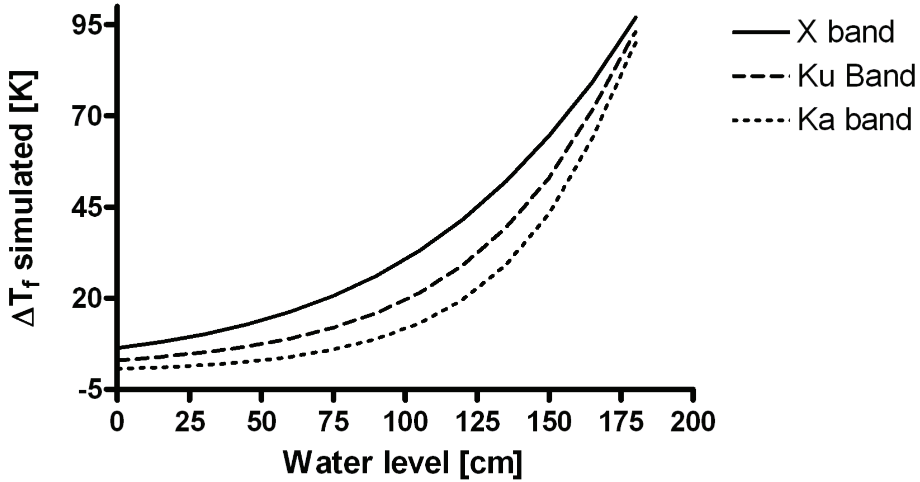

Fig. 5. Polarization difference in flooded marsh (ΔT_f) simulated as a function of water level at X, Ku and Ka Band.

HESSD

8, 2895–2928, 2011

Estimating flood condition from microwave data

M. Salvia et al.

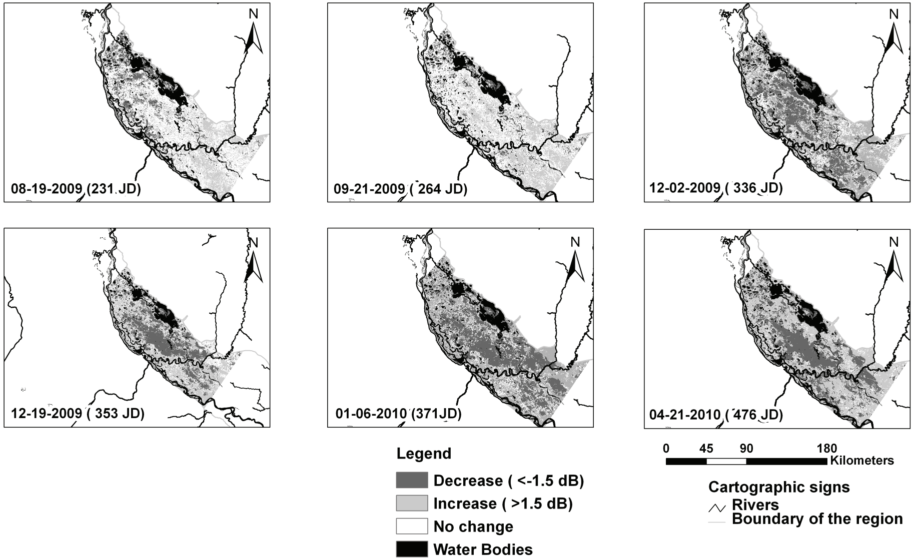

Fig. 6. Maps of σ^0 change derived from ASAR images for six dates. Julian dates starting from 1 January 2009: 231, 264, 336 (top figures), 353, 371, 476 (bottom figures).

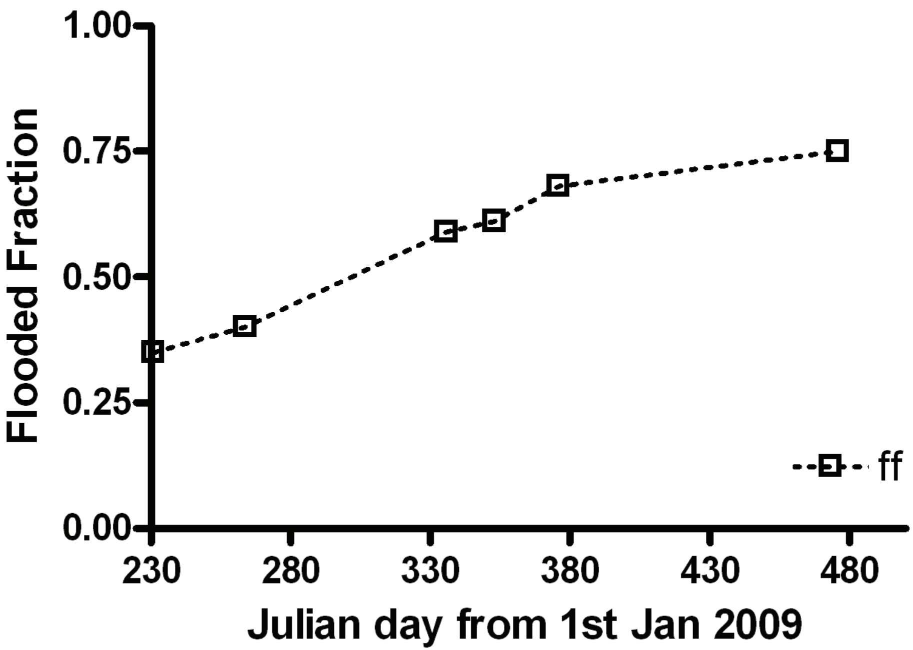

Fig. 7. Fraction of flooded area estimated from ASAR images for six dates.

HESSD
8, 2895–2928, 2011

Estimating flood condition from microwave data

M. Salvia et al.

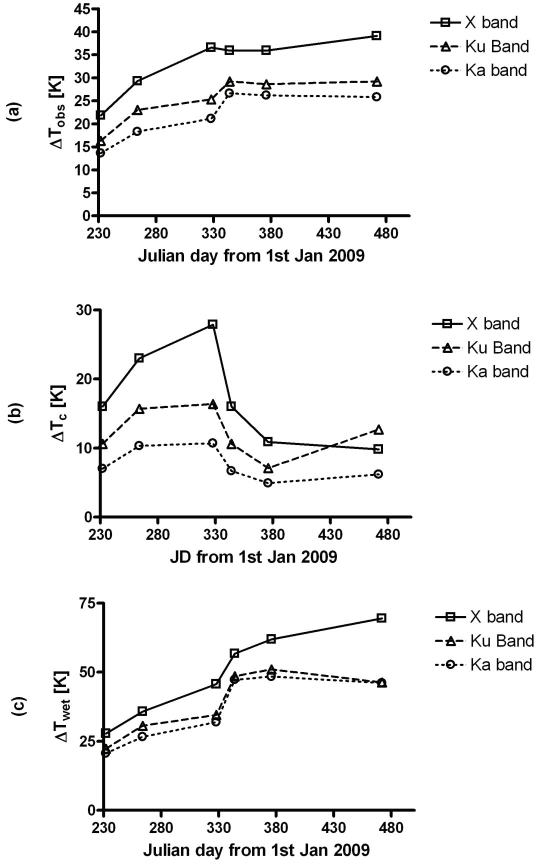

Fig. 8. Polarization differences as a function of time for the three AMSR-E considered bands. **(a)** Overall measured ΔT_{obs}, **(b)** continent ΔT_{c}, **(c)** wetland ΔT_{wet}.

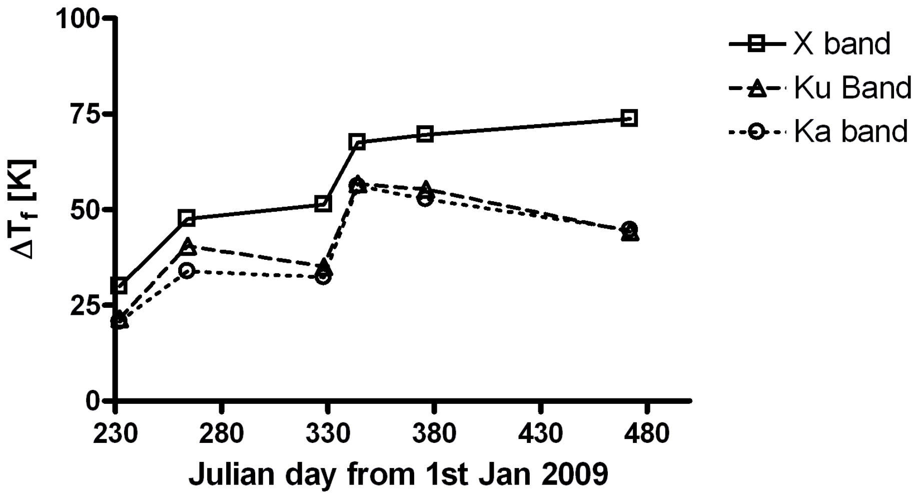

Fig. 9. ΔT flooded as a function of time for the three frequencies.

HESSD
8, 2895–2928, 2011

Estimating flood condition from microwave data

M. Salvia et al.

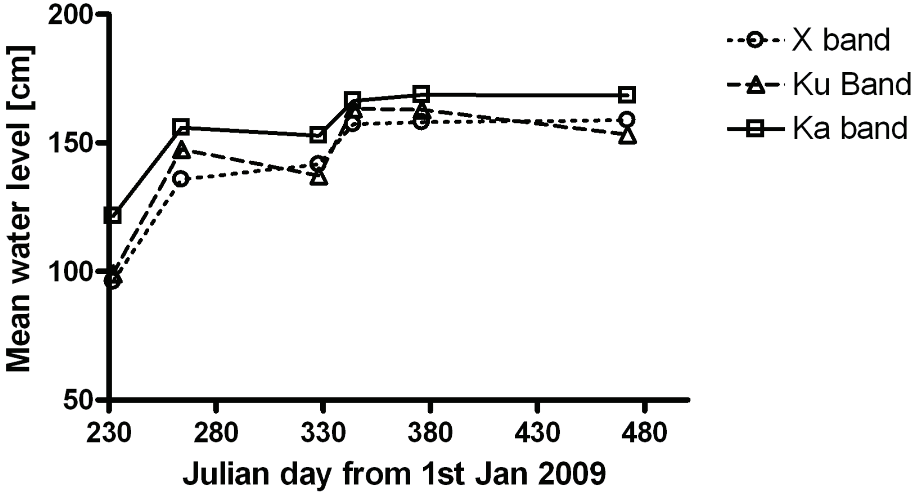

Fig. 10. Mean water level within the studied floodplain area as a function of time, estimated using ΔT_f values (Fig. 9) and model simulations (Fig. 5).

HESSD
8, 2895–2928, 2011

Estimating flood condition from microwave data

M. Salvia et al.